

Article

# Tube Expansion by Single Point Incremental Forming: An Experimental and Numerical Investigation

Carlos Suntaxi <sup>1,2</sup>, Gabriel Centeno <sup>2,\*</sup>, M. Beatriz Silva <sup>3</sup>, Carpóforo Vallellano <sup>2</sup> and Paulo A. F. Martins <sup>3</sup>

<sup>1</sup> Departamento de Ingeniería Mecánica, Facultad de Ingeniería Mecánica, Escuela Politécnica Nacional, Ladrón de Guevara E11-253, Quito P.O. Box 17-01-2759, Ecuador; segundo.suntaxi@epn.edu.ec

<sup>2</sup> Department of Mechanical and Manufacturing Engineering, School of Engineering, University of Seville, Camino de los Descubrimientos s/n, 41092 Seville, Spain; carpofo@us.es

<sup>3</sup> IDMEC, Instituto Superior Técnico, Universidade de Lisboa, Av. Rovisco Pais, 1049-001 Lisboa, Portugal; beatriz.silva@tecnico.ulisboa.pt (M.B.S.); pmartins@tecnico.ulisboa.pt (P.A.F.M.)

\* Correspondence: gaceba@us.es; Tel.: +34-954-485-965

**Abstract:** In this paper, we revisit the formability of tube expansion by single point incremental forming to account for the material strain hardening and the non-proportional loading paths that were not taken into consideration in a previously published analytical model of the process built upon a rigid perfectly plastic material. The objective is to provide a new insight on the reason why the critical strains at failure of tube expansion by single point incremental forming are far superior to those of conventional tube expansion by rigid tapered conical punches. For this purpose, we replaced the stress triaxiality ratio that is responsible for the accumulation of damage and cracking by tension in monotonic, proportional loading paths, by integral forms of the stress triaxiality ratio that are more adequate for the non-proportional paths resulting from the loading and unloading cycles of incremental tube expansion. Experimental and numerical simulation results plotted in the effective strain vs. stress triaxiality space confirm the validity of the new damage accumulation approach for handling the non-proportional loading paths that oscillate cyclically from shearing to biaxial stretching, as the single point hemispherical tool approaches, contacts and moves away from a specific location of the incrementally expanded tube surface.

**Keywords:** single point incremental forming; tube expansion; formability; fracture; stress-triaxiality



**Citation:** Suntaxi, C.; Centeno, G.; Silva, M.B.; Vallellano, C.; Martins, P.A.F. Tube Expansion by Single Point Incremental Forming: An Experimental and Numerical Investigation. *Metals* **2021**, *11*, 1481. <https://doi.org/10.3390/met11091481>

Academic Editor: Zhengyi Jiang

Received: 18 August 2021

Accepted: 14 September 2021

Published: 17 September 2021

**Publisher's Note:** MDPI stays neutral with regard to jurisdictional claims in published maps and institutional affiliations.



**Copyright:** © 2021 by the authors. Licensee MDPI, Basel, Switzerland. This article is an open access article distributed under the terms and conditions of the Creative Commons Attribution (CC BY) license (<https://creativecommons.org/licenses/by/4.0/>).

## 1. Introduction

The route for characterizing the sheet formability limits started in the late 1960s when Keeler [1] and Goodwin [2] developed the circle grid analysis (CGA) technique for determining the in-plane strains on the surface of sheet metal formed parts. The use of principal strain space to plot these strains and to identify their critical values at the onset of failure by Embury and Duncan [3] in the early 1980s paved the way to what they called “formability maps”, which are nowadays known as the forming limit diagrams (FLDs) [4].

A typical FLD for a sheet metal forming material is built on three different types of failure limit curves [5]: (i) the forming limit curve (FLC) corresponding to failure by necking, (ii) the fracture forming limit lines corresponding to failure by cracking and (iii) the wrinkling limit curve (WLC) delimiting the onset of wrinkling in the lower left-hand of the second quadrant. In sheet metal forming, there are two fracture forming lines corresponding to crack opening by tension (mode I of fracture mechanics, hereafter referred to as FFL) and crack opening by in-plane shear (mode II of fracture mechanics, hereafter referred to as SFFL) [6]. The experimental determination of the FFLs and SFFLs was comprehensively explained by the authors in previous publications [4,5], who also described the different methods and procedures to obtain the FLCs.

The route for establishing the formability limits of tube materials starts with the determination of the onset of necking (FLC) by means of tube of hydroforming [7,8]. No

methodologies for characterizing the crack opening modes and determining the fracture forming lines were proposed until 2016, when Centeno et al. [9] utilized CGA to plot the FLC and the FFL corresponding to tube cracking by tension.

Subsequent research work combining numerical methods, digital image correlation (DIC) and making use of a broader range of tube forming processes comprising expansion [10], inversion [11] and bulging [12] allowed obtaining the FLC and the FFL of tube materials for a wider range of strain paths running from uniaxial tension up to equal biaxial stretching (e.g., from strain ratios  $\beta = d\epsilon_2/d\epsilon_1$  ranging between  $-1/2$  to 1). These efforts were recently complemented by the work of Magrinho et al. [13], who proposed an experimental procedure to determine the SFFL of tube materials (i.e., the fracture forming limit line corresponding to tube cracking by in-plane shear).

In view of the aforementioned work, recent developments in incremental tube expansion, reduction, wall grooving and hole flanging using a single point hemispherical tool by Wen et al. [14] and Movahedinia et al. [15] raise the question of whether their deformation mechanics and formability limits remain the same as those of conventional tube forming processes. The answer to this question was firstly addressed by Cristino et al. [16], who presented an analytical model based on membrane analysis for tube expansion by single point incremental forming (hereafter referred to as incremental tube expansion). The model reveals the main differences between conventional and incremental tube expansion in terms of stress/strain states and damage accumulation to explain the greater formability of incremental tube expansion compared to that of conventional tube expansion with a rigid tapered conical punch.

The analytical model of Cristino et al. [16] is based on a rigid, perfectly plastic tube material and assumes near-proportional (equal biaxial stretching) experimental strain loading paths in principal strain space to facilitate algebraic treatment.

Under these circumstances, it is important to revisit the accumulation of damage by means of a numerical simulation model capable of accounting for material strain hardening and for the loading/unloading cycles of incremental tube expansion. In this paper, we provide a novel perspective on the formability and failure of incremental tube forming processes subjected to non-proportional loading. We analyze different methodologies to account for stress triaxiality and accumulation of damage, and discuss if the FFLs of tube materials determined by means of conventional tube forming processes subjected to near proportional loading paths are still valid for incremental tube expansion characterized by non-proportional loading paths that oscillate cyclically from shearing to biaxial stretching, as the single point hemispherical tool approaches, contacts and moves away from a specific location of the plastically deformed tube surface.

Experimental and numerical simulation results plotted in the space of effective strain vs. stress triaxiality [17] give support to the discussion, which is of paramount importance to infer about the FFLs of tubes being material properties, in contrast to their FLCs, which are dependent on the applied loading paths.

## 2. Methods and Procedures

The investigation was carried out in AA6063-T6 extruded aluminum tubes with an outer radius  $r_0 = 20$  mm and a wall thickness  $t_0 = 2$  mm. The first part of this section summarizes the methods and procedures that were utilized to determine the material flow curve and the formability limits by necking (FLC) and by fracture under tension (FFL) using conventional tube forming processes. The data provided in the figures were retrieved from previous publications of the authors [9–12].

In the second part of this section, we present the experimental testing conditions of incremental tube expansion, describe the methodology that was used to determine the strain paths using circle grid analysis (CGA), provide an analytical framework to transform the formability limits from principal strain space into the effective strain vs. stress-triaxiality space and summarize the numerical modelling conditions utilized in finite element analysis.

### 2.1. Flow Curve

The flow curve of the AA6063-T6 tubes is shown in Figure 1 and was obtained by merging the stress–strain evolutions that were previously obtained by the authors using tensile and stack compression tests [9]. Tensile tests were carried out in specimens machined out from the tube longitudinal direction and provided the material stress response for values of effective strain below 0.23 (refer to the vertical dashed line). Stack compression tests were performed in cylindrical specimens that were assembled by pilling up disks that were also machined out from the supplied tubes and allowed characterizing the strain hardening behavior of the tube material for the remaining values of effective strain.

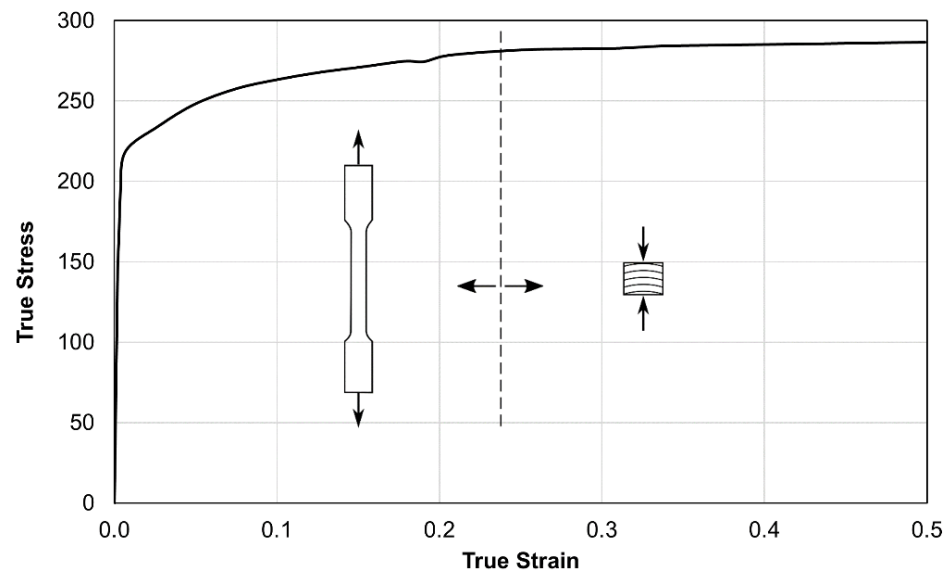


**Figure 1.** Flow curve of the aluminum AA6063T6 tubes (adapted from [9]).

### 2.2. Formability Limits by Necking and Fracture

Figure 2 shows the formability limits of the aluminum AA6063-T6 tubes by necking (FLC) and by fracture under tension (FFL) in principal strain space. Determination of the FLC required measuring the strain paths of conventional tube expansion, inversion and bulging by means of digital image correlation (DIC) and combining these results with time-dependent and force-dependent methodologies that were specifically developed by the authors for tube materials [11,12]. Determination of the FFL required measuring the wall thickness of the tube cracked regions by optical microscopy (D software version 5.11.01, NIS-Elements, Tokyo, Japan) to obtain the “gauge length” strains at fracture. Information about the different tests, methods and procedures that were used by the authors to determine the FLCs and FFLs of tube materials is given in Magrinho et al. [12].

Figure 2 also includes the strain loading path obtained in conventional tube expansion with a rigid tapered conical punch having a semi-angle of  $15^\circ$ , which was previously obtained by the authors [12] and will be used for reference purposes throughout this paper. As seen, the in-plane strains of conventional tube expansion at the onset of necking  $(\epsilon_{1n}, \epsilon_{2n}) = (-0.25, 0.41)$  are very close to the FLC, and the in-plane fracture strains  $(\epsilon_{1f}, \epsilon_{2f}) = (-0.25, 0.71)$  are exactly on top of the FFL.

The formability limits shown in Figure 2 can alternatively be plotted in the effective strain vs. stress triaxiality space (Figure 3). The transformation of the formability limits from principal strain space into this other space can be carried out analytically by assuming linear, proportional strain paths under plane stress loading conditions ( $\sigma_t = \sigma_3 \approx 0$ ). Plane stress loading conditions are commonly assumed in the analytical modelling of sheet and thin-wall tube forming [12,18].

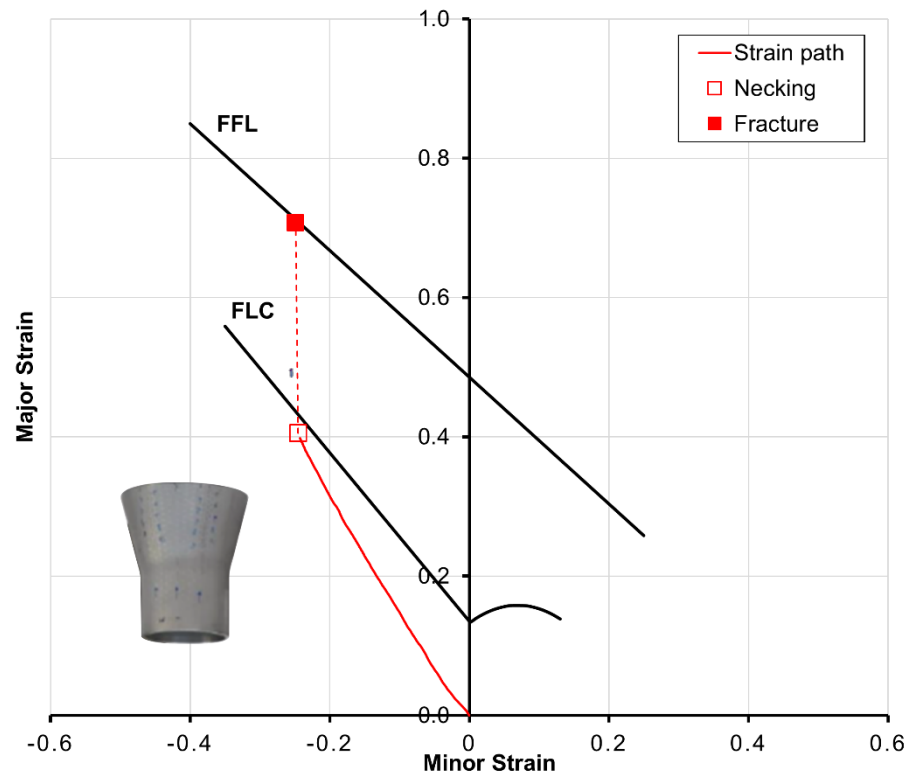


**Figure 2.** Forming limit curve (FLC) and fracture forming limit (FFL) line of the aluminum AA6063-T6 tube in principal strain space. The red line represents the experimental strain loading path of conventional tube expansion with a rigid tapered conical punch having a semi-angle of  $15^\circ$  (adapted from [12]).

For this purpose, let us consider, for example, the tube material to be isotropic and to follow the von Mises yield criterion, so that its effective stress  $\bar{\sigma}$  and effective strain  $d\bar{\epsilon}$  are given by:

$$\bar{\sigma} = \sqrt{\sigma_1^2 - \sigma_1\sigma_2 + \sigma_2^2} \quad (1)$$

$$d\bar{\epsilon} = \frac{2}{\sqrt{3}} \sqrt{d\epsilon_1^2 + d\epsilon_1 d\epsilon_2 + d\epsilon_2^2} \quad (2)$$

Then, applying the Levy–Mises constitutive equations, one obtains the following relation between the stress triaxiality ratio  $\eta = \sigma_m / \bar{\sigma}$  and the slope  $\beta = d\epsilon_2 / d\epsilon_1$  of the strain path [9]:

$$\eta = \frac{1 + \beta}{\sqrt{3} \sqrt{1 + \beta + \beta^2}} \quad (3)$$

The above equation together with the following modified version of Equation (2) to include the slope  $\beta$  in the effective strain,

$$\bar{\epsilon} = \frac{2}{\sqrt{3}} \sqrt{1 + \beta + \beta^2} \epsilon_1, \quad (4)$$

allows accomplishing the above-mentioned transformation of the FLC from principal strain space into the effective strain vs. stress triaxiality space (Figure 3).

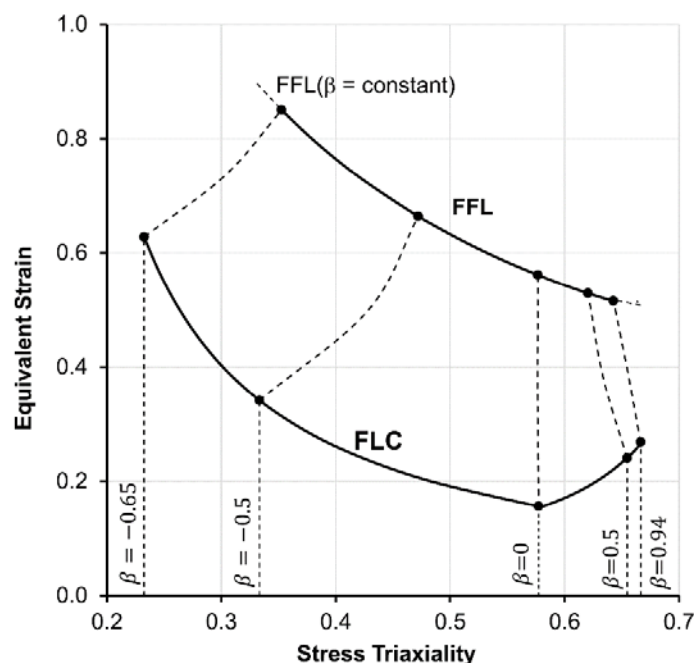


**Figure 3.** Forming limit curve (FLC) and fracture forming limit (FFL) line of the aluminum AA6063-T6 tube in the effective strain vs. stress triaxiality space, obtained from analytical transformation assuming material isotropy, linear strain paths and plane stress loading conditions.

The transformation of the FFL from principal strain space into the effective strain vs. stress triaxiality space requires consideration of the experimentally observed strain path deviation towards plane strain deformation conditions at the onset of necking (FLC); see, for instance, Martinez-Donaire et al. [19]. In case of the effective strain  $\bar{\epsilon}$ , this is realized by modifying Equation (4) to account for the two piecewise linear strain paths involving the initial path (up to necking) with a given slope  $\beta$  and the final path (from necking to fracture) with a slope  $\beta = 0$  resulting from strain localization in the tube material:

$$\bar{\epsilon}_f = \int_0^{\bar{\epsilon}_n} d\bar{\epsilon} + \int_{\bar{\epsilon}_n}^{\bar{\epsilon}_f} d\bar{\epsilon} = \frac{2}{\sqrt{3}} \left[ \epsilon_{1f} + \left( \sqrt{1 + \beta + \beta^2} - 1 \right) \left( \epsilon_{2f} / \beta \right) \right] \tag{5}$$

In the above equation,  $\epsilon_{1f}$  and  $\epsilon_{2f}$  are the major and minor in-plane strains at fracture, and  $\bar{\epsilon}_f$  is the effective strain at fracture.

In case of the stress triaxiality  $\eta$ , the transformation is carried out in accordance with Martinez-Donaire et al. [19], who introduced an integral form  $\bar{\eta}_f$ , named average-stress triaxiality at fracture, that accounts for stress triaxiality in an average sense over the two piecewise linear strain paths:

$$\bar{\eta}_f = \frac{1}{\bar{\epsilon}_f} \int_0^{\bar{\epsilon}_f} \frac{\sigma_m}{\bar{\sigma}} d\bar{\epsilon} = \frac{1}{\bar{\epsilon}_f} \left( \int_0^{\bar{\epsilon}_n} \frac{\sigma_m}{\bar{\sigma}} d\bar{\epsilon} + \int_{\bar{\epsilon}_n}^{\bar{\epsilon}_f} \frac{\sigma_m}{\bar{\sigma}} d\bar{\epsilon} \right) = \frac{\sqrt{3}}{3} \left[ \frac{\epsilon_{1f} + \epsilon_{2f}}{\epsilon_{1f} + \left( \sqrt{1 + \beta + \beta^2} - 1 \right) \left( \epsilon_{2f} / \beta \right)} \right] \tag{6}$$

The FLC and FFL resulting from the above-mentioned analytical transformation procedure are shown in Figure 3 and are slightly different from those obtained by Magrinho et al. [12] due to the following two main reasons. First, the authors made use of the von Mises yield criterion instead of the Hosford yield criterion that was utilized by Magrinho et al. [12]. Second, Magrinho et al. [12] transformed the FFL from principal strain space into the effective strain vs. stress triaxiality space by replacing the strains at fracture directly on Equations (3) and (4) instead of using the two piecewise linear strain path approach given by Equations (5) and (6), i.e., without considering the kink in the strain loading path from necking towards fracture.

To conclude, it is worth mentioning that the main reason why the Hosford yield criterion was not utilized in this work was due to its unavailability in the commercial finite element computer program utilized by the authors. Hill's 48 yield criterion was not considered as well because of the difficulty in obtaining the Lankford's coefficient at  $45^\circ$  in a tube, and because Cristino et al. [16] achieved good analytical estimates of material flow neglecting anisotropy.

### 2.3. Incremental Tube Expansion

The experiments in incremental tube expansion were performed in a Deckel Maho CNC machining center equipped with a single point hemispherical tool ( $r_{tool} = 5$  mm) made from a cold working tool steel (120WV4-DIN) hardened and tempered to 60 HRC. The bottom tube end of the specimens was fixed to prevent sliding and rotation, and the tool path was programmed to perform a multi-stage incremental forming sequence consisting of an upward helical trajectory with a constant semi-angle  $\Psi = 15^\circ$  (Figure 4a). The pitch  $p$  between two consecutive stages was set to 2 mm and the initial tool depth at the beginning of the first stage was set to 2 mm with respect to the upper tube end (Figure 3b). Table 1 summarizes the main process parameters.

Three different tests were performed under the above-mentioned experimental conditions and a total of eight forming stages were needed for each test to observe of an incipient failure by fracture close to the plastically deformed tube end (Figure 3c), as is later discussed in the paper.

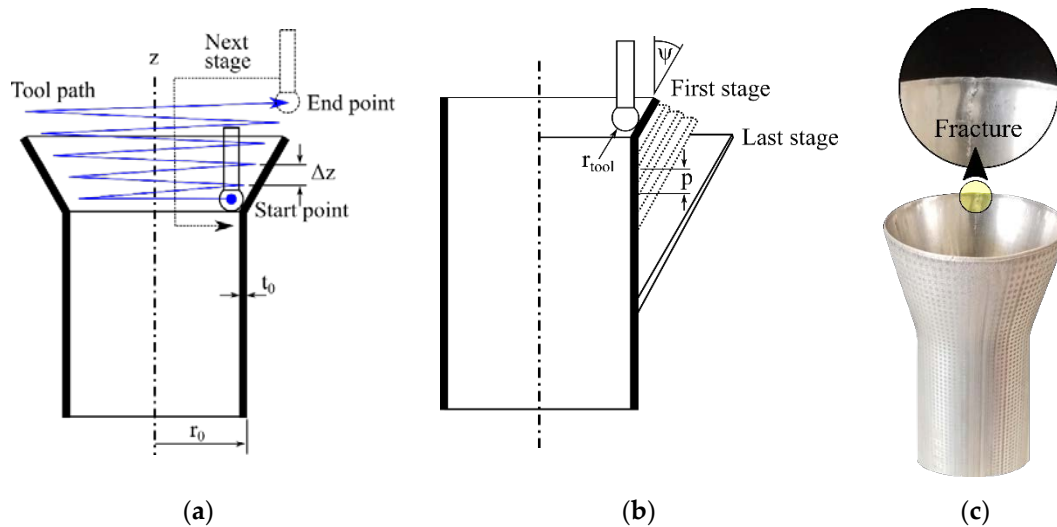


**Figure 4.** Schematic representation of incremental tube expansion showing (a) the single point hemispherical tool path and (b) the multi-stage forming strategy. A photograph of a specimen after eight forming stages is included in (c) together with a detail showing the final cracked surface.

**Table 1.** Main parameters used in the incremental tube expansion tests.

Parameter	Value
Tool radius $r_{tool}$	5 mm
Pitch $p$	2 mm
Step down $\Delta z$	0.2 mm
Semi-angle of inclination $\Psi$	$15^\circ$
Feed rate	1000 mm/min

### 2.4. Strain Measurement Using Circle Grid Analysis

The in-plane strains of the incrementally expanded tubes were determined by CGA using the automatic measurement system ARGUS<sup>®</sup> v.6.2 by GOM<sup>™</sup> equipped with a camera having a resolution of  $1624 \times 1236$  pixels. For this purpose, the outer tube surfaces

were electrochemically etched with a grid of circles with 0.75 mm of diameter and a distance between centers of 1.5 mm.

Measurement and classification of the deformed circles into different colors by ARGUS at the end of incremental tube expansion (Figure 5a) allowed determining the in-plane distribution of strains along the longitudinal direction from the undeformed lower tube region to the upper end of the plastically expanded tube surface (Figure 5b). The results for a typical longitudinal cross section marked with a black line in Figure 5a are given by the corresponding black line in principal strain space (Figure 5b).

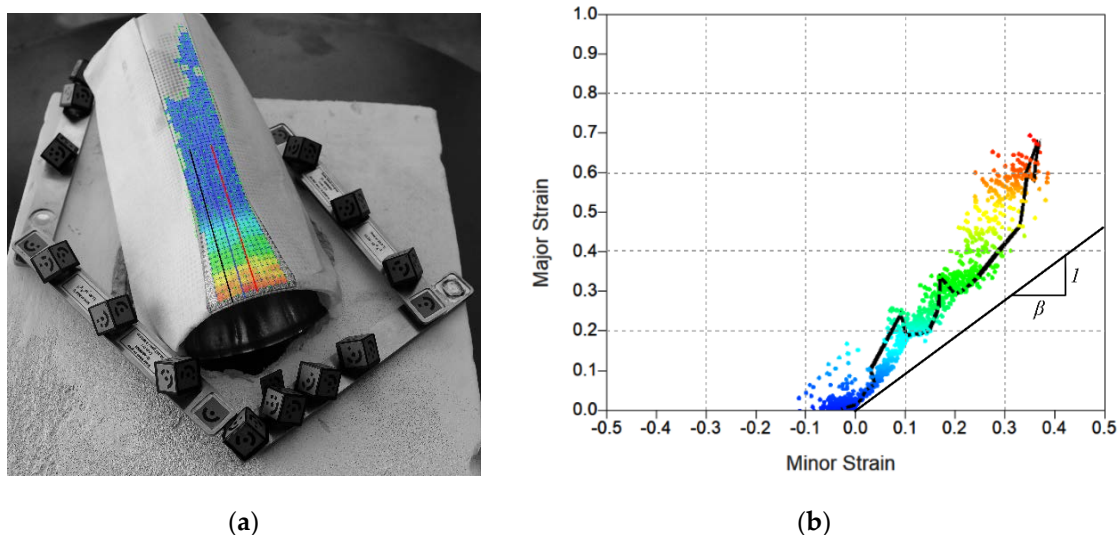


**Figure 5.** (a) Experimental determination of the in-plane strains by CGA using the automatic measuring system ARGUS®, and (b) representation of these strains in principal strain space.

### 2.5. Numerical Modelling

Numerical modelling of the conventional and incremental tube expansion processes was carried out with the commercial finite element computer program DEFORM™-3D. DEFORM™-3D was chosen due its capability to obtain a good agreement between numerical and experimental strains in incremental sheet forming processes [20,21].

The tube material was assumed as isotropic, elastic and plastic, and its initial geometry was discretized by means of solid tetrahedral elements. Tube material properties were taken from a previous work of the authors [9]. The tools were modelled as rigid (non-deformable) bodies and discretized by means of spatial triangular elements.

A penalty contact algorithm was utilized to model the interaction between the tools and the tube material.

Discretization of the tube and tool in case of conventional tube expansion with a rigid tapered conical punch took advantage of the rotational symmetry conditions of the process to create a simple three-dimensional model built upon an angular sector of 18° (1/20 of the full three-dimensional model). A total of 11,530 tetrahedral elements were utilized with an average side length of 1 mm and a reduced side length of 0.25 mm in the upper tube regions where mesh refinement was needed. Figure 6 shows the initial and final deformed meshes with the predicted contour of effective strain at the end of the process.

Typical CPU time to complete the numerical modelling of conventional tube expansion was approximately 3 min in a personal computer equipped with an Intel I7-4749 CPU (3.6 GHz) processor.

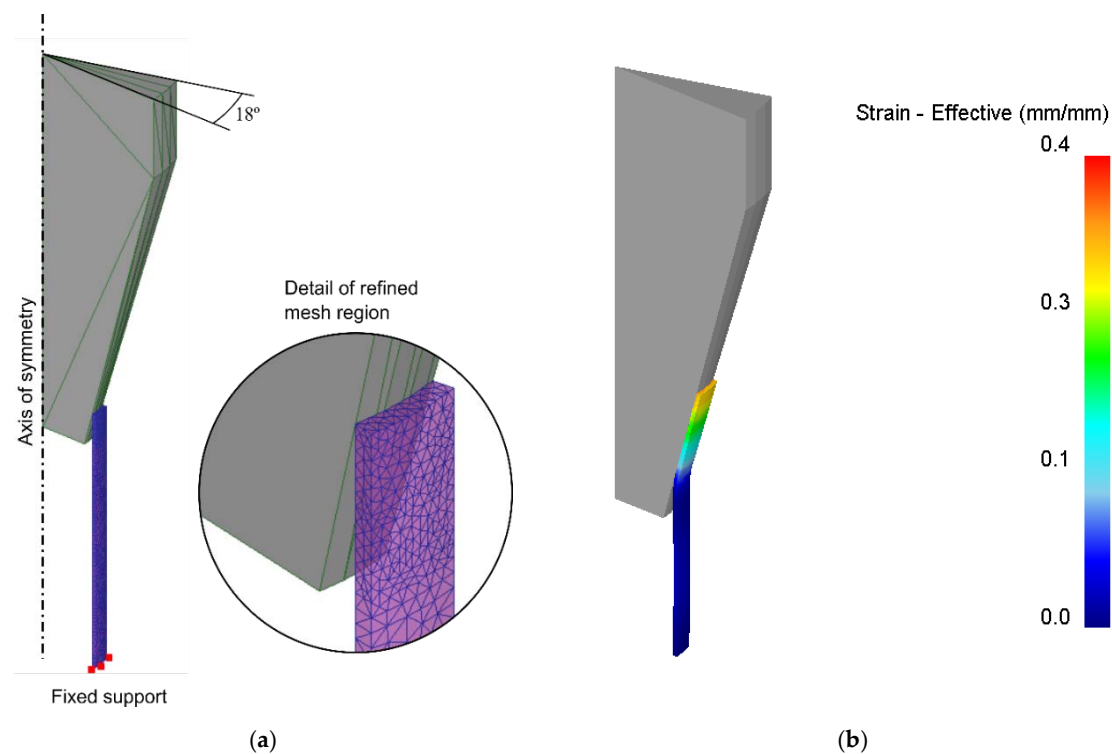


**Figure 6.** Finite element modeling of conventional tube expansion with a rigid tapered conical punch having a semi-angle of  $15^\circ$ . (a) Initial mesh with a detail of mesh refinement and (b) predicted distribution of effective strain at the end of the process.

Discretization of the tube material and of the single point hemispherical tool in case of incremental tube expansion required a full three-dimensional finite element model. The initial mesh consisted of 50,000 tetrahedral elements distributed along a finer mesh region at the upper tube end, which initially comes into contact with the tool, and a coarser mesh region for the remaining regions of the tube (Figure 7a). The final mesh at the end of the process (Figure 7b) consisted of approximately 120,000 tetrahedral elements due to several remeshings (based on critical element distortion) that were automatically performed to keep the numerical simulation from stopping because of excessive element distortion.

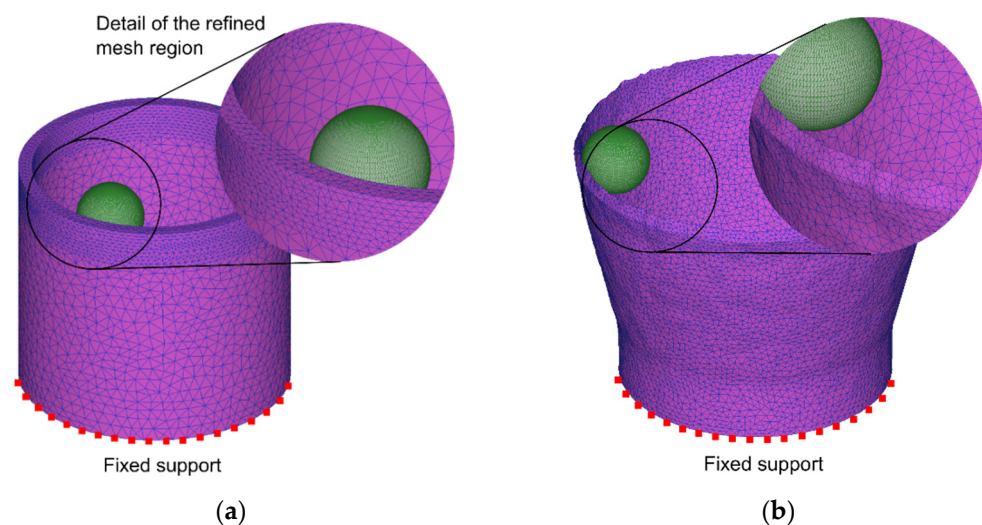


**Figure 7.** Finite element modeling of incremental tube expansion. (a) Initial mesh and (b) final mesh after eight forming stages.



at the vicinity of the incipient cracking zone and calculating the through-thickness strain  $\varepsilon_{3f}$  at fracture to obtain the ‘gauge length’ strains  $(\varepsilon_{1f}, \varepsilon_{2f})$ .

This alternative procedure was necessary because neither ARGUS<sup>®</sup> nor DEFORM<sup>™</sup>-3D could provide the in-plane strains at fracture. In fact, the application of circle grids with very small diameters to obtain the in-plane strains in the cracked region by means of ARGUS<sup>®</sup> is not feasible because it creates measurement problems and delivers values that cannot be considered fracture strains due to inhomogeneous material deformation around the cracks. Similar problems exist in finite element modelling with the use of very refined meshes in the regions where the cracks are likely to be triggered, plus the additional difficulty resulting from these results being sensitive to mesh size.

Under these circumstances, the authors had to measure the tube wall thickness in a NICON<sup>®</sup> SMZ800 optical microscope equipped with a NIS-Elements<sup>®</sup> D software version 5.11.01. Figure 9 shows a longitudinal cross-section detail after completion of the incremental tube expansion process with the corresponding evolution of thickness along the longitudinal direction (starting from the upper tube end). As seen, two different regions may be distinguished: (i) a first region (labeled as “I”) located near the upper tube end that is characterized by a sharp decrease in wall thickness and (ii) a second region (labelled as “II”), in which the wall thickness progressively increases, as the distance to the upper tube end increases and approaches the undeformed region (not subjected to incremental expansion), along which the tube wall thickness  $t_0 = 2$  mm remained unchanged.

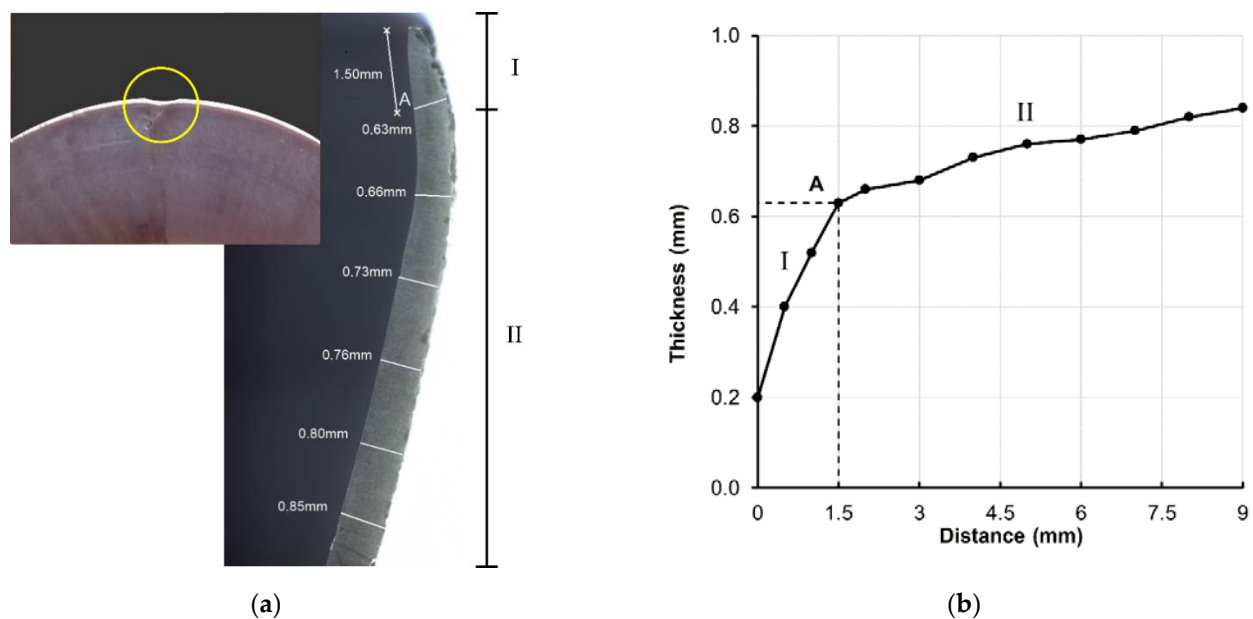


**Figure 9.** (a) Detail of a tube section after the incremental expansion and (b) evolution of the tube wall thickness with the longitudinal distance to the upper tube end.

Two main conclusions can be inferred from Figure 9: (i) failure by cracking is not preceded by necking and (ii) failure by cracking is related to a sharp decrease in the tube wall thickness in a small region “I” subjected to a great amount of straining. As seen, there is no localized thickness reduction in the detail of the tube section after the last forming stage of incremental expansion. This observation combined with the monotonic increase in the strain loading path up to fracture shown in Figure 8 (refer to the black triangular markers) allow concluding that failure occurs without previous necking.

A closer observation of the tube wall thickness within region “I” confirms the existence of micro-cracks along its length, as it was previously stated by Cristino et al. [16], and justifies the reason why the experimental determination of the “gauge length” strains

$(\varepsilon_{1f}, \varepsilon_{2f})$  at fracture was made at point “A” (Figure 9) located 1.5 mm away from the upper tube end, in the transition between regions “I” and “II”.

The finite element predicted evolution of the in-plane strains at point “A” for each individual stage of the incremental tube expansion process is shown in Figure 10. As mentioned before, the “gauge length” strains  $(\varepsilon_{1f}, \varepsilon_{2f})$  at fracture (refer to the black solid triangular marker) were not obtained by finite elements and their determination made use of the tube wall thickness value at point “A” (Figure 9b) to calculate the through-thickness strain  $\varepsilon_{3f}$  at fracture.

$$\varepsilon_{3f} = \ln \frac{t_f}{t_0} = \ln \frac{0.63}{2} = -1.16 \quad (7)$$

Then, assuming material incompressibility and the final slope  $\beta$  of the strain loading path to remain identical to that of the last piecewise linear path obtained by ARGUS<sup>®</sup> (Figure 8), it was possible to determine the ‘gauge length’ strains  $(\varepsilon_{1f}, \varepsilon_{2f})$  at fracture, as follows:

$$\beta = \frac{\varepsilon_2}{\varepsilon_1} = 0.54 \quad \rightarrow \quad \varepsilon_{1f} = -\frac{\varepsilon_{3f}}{1 + \beta} = 0.75 \quad , \quad \varepsilon_{2f} = \beta \varepsilon_{1f} = 0.40 \quad (8)$$

The corresponding effective strain at fracture  $\bar{\varepsilon}_f = 1.17$  was obtained from Equation (4) and defines a dashed ellipse of constant effective strain values in principal strain space (refer to both Figures 8 and 9).

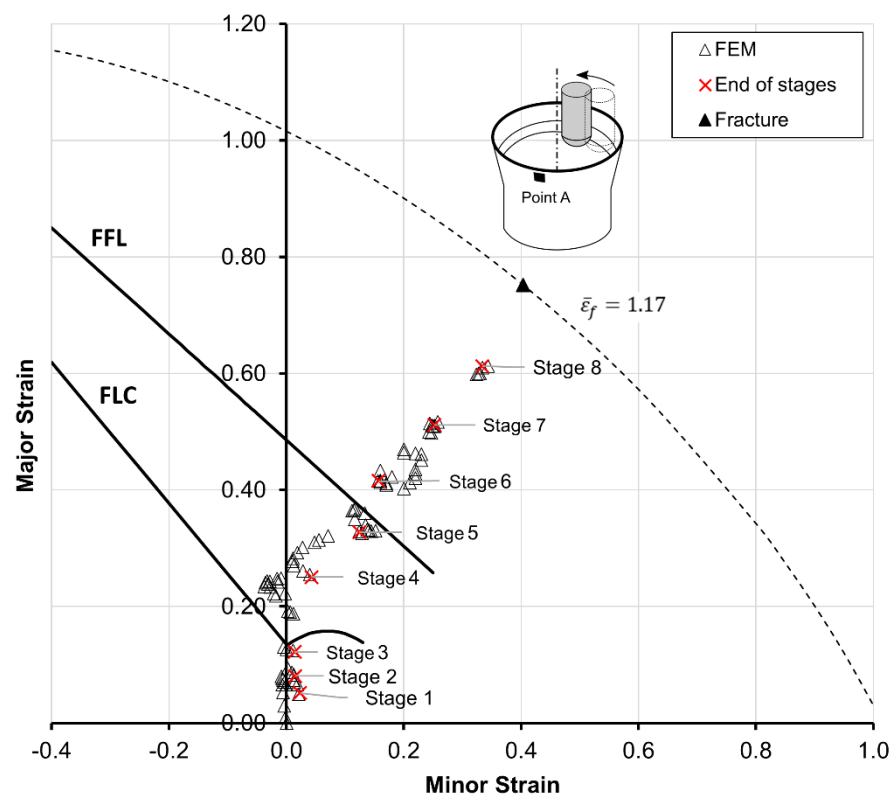


**Figure 10.** Finite element predicted in-plane strains of point A during the eight forming stages of incremental tube expansion.

The comparison of the results obtained for incremental tube expansion against those obtained for conventional tube expansion with a rigid tapered conical punch [9–12] allowed identifying two main differences regarding material flow and cracking. First, incremental tube expansion is performed under biaxial stretching conditions, whereas conventional tube expansion subjects the material to near pure tension. Second, both processes fail by

tensile stresses (opening mode I), but while fracture in incremental tube expansion is not preceded by necking, that is not the case in conventional tube expansion, in which fracture is preceded by localized necking.

Even though all the experimental and theoretical results presented in this section are consistent and compatible, there is a fundamental problem arising from the fact that in-plane strains of incremental tube expansion are far greater than the threshold admissible values given by the FFL. Because the FFL is a material property, whose values cannot be surpassed, Cristino et al. [16] put forward the possibility of the FFL having an upward curvature in the first quadrant of principal strain space to accommodate the values in excess (i.e., to accommodate the in-plane strains located above the straight line falling from left to right), but they did not provide evidence for this type of tube material.

In connection to this, it is worth noticing that recent published works in incremental sheet forming also report the existence of strain paths that go beyond the FFL determined by means of conventional sheet forming tests with proportional strain paths [22].

The following section focuses on this problem and aims at providing an explanation for the reason why the critical strains of incremental tube expansion at fracture are far superior to those of conventional tube expansion that is simultaneously compatible with the FFL being a material property, whose threshold values cannot be surpassed by any type of loading. The explanation will make use of the effective strain vs. stress triaxiality space instead of the principal strain space.

### 3.2. FFL and Stress Triaxiality under Non-Proportional Paths

Damage accumulation associated to growth and coalescence of voids subjected to tensile normal stresses (Mode I) accounts for the dilatational effects related to stress triaxiality  $\eta = \sigma_m / \bar{\sigma}$ , in the form of a weighted integral form of the effective plastic strain [23–25].

$$D = \int_0^{\bar{\epsilon}} \frac{\sigma_m}{\bar{\sigma}} d\bar{\epsilon} \quad (9)$$

The critical damage  $D_{crit}$  at the onset of fracture (FFL) corresponds to the maximum admissible accumulated value of effective strain  $\bar{\epsilon} = \bar{\epsilon}_f$  for a given strain path.

The accumulation of damage  $D$  in principal strain space often distinguishes between two different types of strain paths: (i) linear, proportional strain paths (Figure 11a) and (ii) non-proportional strain paths, which are often discretized through a series of piecewise linear strain paths for calculation purposes (Figure 11b).

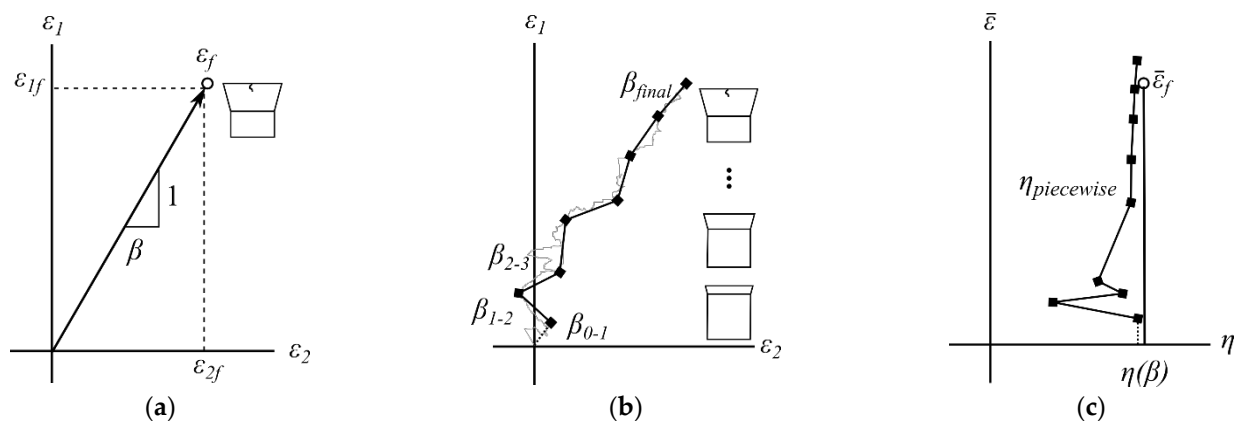


**Figure 11.** (a) Linear, proportional strain path in principal strain space, (b) non-proportional strain path discretized through a series of piecewise linear strain paths in principal strain space, (c) representation of the strain paths (a,b) in the effective strain vs. stress triaxiality space.

As shown in Figure 11c, the application of Equations (3) and (4) to linear, proportional strain paths, characterized by a constant slope  $\beta = d\epsilon_2 / d\epsilon_1$  (Figure 11a), gives rise to

vertical lines  $\eta = \eta_p$  in the effective strain vs. stress triaxiality space. In contrast, the application of Equations (3) and (4) to non-proportional, piecewise linear strain paths with different slopes  $\beta_i$ , gives rise to piecewise linear evolutions  $\bar{\varepsilon} = f(\eta_i)$  (hereafter referred to as  $\eta_{piecewise}$  based evolutions) in the effective strain vs. stress triaxiality space.

The experimental strain paths disclosed in Figure 8 allow concluding that tube expansion by a rigid tapered conical punch subject the material to linear, proportional (or near proportional) strain paths, whereas incremental tube expansion subjects the material to non-proportional strain paths. The picture inserts of Figure 11a,b are drawn in accordance with this conclusion.

However, the strain paths determined by CGA using the automatic measurement system ARGUS<sup>®</sup> must be seen as static results obtained at the end of the incremental tube expansion process (Figure 8), or at the end of each intermediate forming stage (Figure 10). Full characterization of the non-proportional strain paths of incremental tube forming with detailed information on the cyclic oscillations from shearing to biaxial stretching, as the single point hemispherical tool approaches, contacts and moves away from a specific location of the incrementally expanded tube surface can only be obtained through finite element modelling.

Figure 12 provides a schematic representation of a finite element computed non-proportional, cyclic path undergone by a specific tube location in the effective strain vs. stress triaxiality space. Three different evolutions  $\bar{\varepsilon} = f(\eta)$  are considered as a result of the following three approaches to account for the accumulation of damage  $D$  in non-proportional, cyclic paths:

(a) The envelope stress triaxiality  $\eta_{env}$  based approach (Figure 12a).

$$D_{env} = \eta_{env} \bar{\varepsilon} \rightarrow \eta_{env} = \frac{1}{\bar{\varepsilon}} \int_0^{\bar{\varepsilon}} \left( \frac{\sigma_m}{\bar{\sigma}} \right)_{max} d\bar{\varepsilon} \quad (10)$$

where  $(\cdot)_{max}$  stands for the peak values of the stress triaxiality ratio at each cycle (circular path) of the forming tool.

(b) The average positive stress triaxiality  $\bar{\eta}_{pos}$  based approach (Figure 12b).

$$D_{pos} = \bar{\eta}_{pos} \bar{\varepsilon} \rightarrow \bar{\eta}_{pos} = \frac{1}{\bar{\varepsilon}} \int_0^{\bar{\varepsilon}} \langle \frac{\sigma_m}{\bar{\sigma}} \rangle d\bar{\varepsilon} \quad (11)$$

where  $\langle \cdot \rangle$  corresponds to the Macaulay bracket to prevent accumulation of negative damage.

(c) The average stress triaxiality  $\bar{\eta}$  based approach (Figure 12c), where  $\bar{D} = D$  of Equation (9).

$$\bar{D} = \bar{\eta} \bar{\varepsilon} \rightarrow \bar{\eta} = \frac{1}{\bar{\varepsilon}} \int_0^{\bar{\varepsilon}} \frac{\sigma_m}{\bar{\sigma}} d\bar{\varepsilon} \quad (12)$$

where  $\bar{D} = D$  of Equation (9).

The three evolutions  $\bar{\varepsilon} = f(\eta)$  resulting from these approaches are identical in case of linear, proportional strain paths because in such loading conditions,  $D = D_{env} = D_{pos} = \bar{D}$ .

Figure 13 shows the finite element non-proportional, cyclic path of incremental tube forming experienced by point A of Figure 9 and the three different  $\bar{\varepsilon} = f(\eta)$  evolutions that result from the integral forms of stress triaxiality  $\eta_{env}$ ,  $\bar{\eta}_{pos}$  and  $\bar{\eta}$  given by Equations (10)–(12). The linear piecewise  $\eta_{piecewise}$  based evolution resulting from the experimental in-plane strains obtained by ARGUS<sup>®</sup> and by the linear, proportional, equal biaxial stretching  $\eta_p$  based evolution are included for comparison purposes.

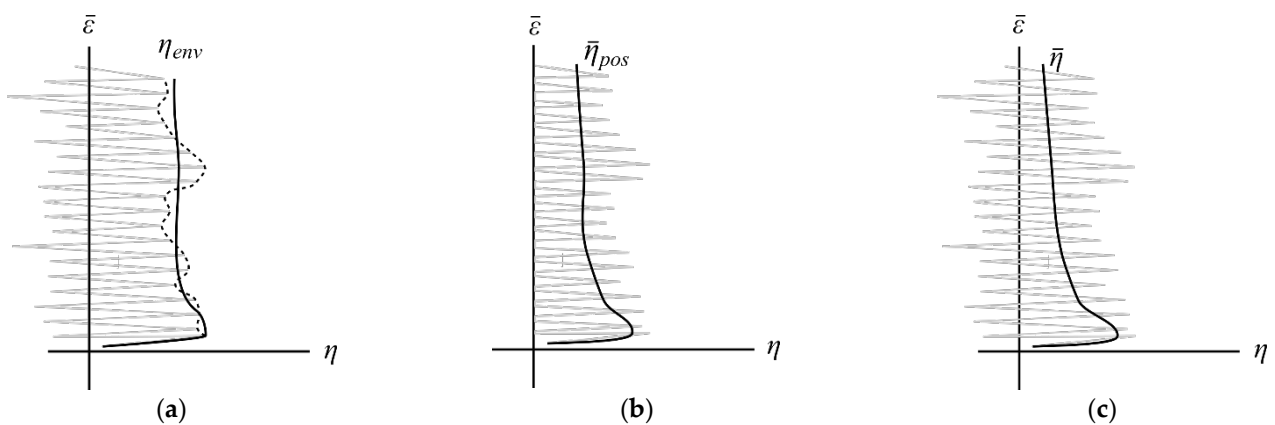


**Figure 12.** Schematic representation of the non-proportional, cyclic path of incremental tube expansion experienced by an arbitrary tube location with a plot of the  $\bar{\epsilon} = f(\eta)$  evolutions based on the three different integral forms of stress triaxiality: (a) envelope stress triaxiality  $\eta_{env}$ , (b) average positive stress triaxiality  $\bar{\eta}_{pos}$  and (c) average stress triaxiality  $\bar{\eta}$ .

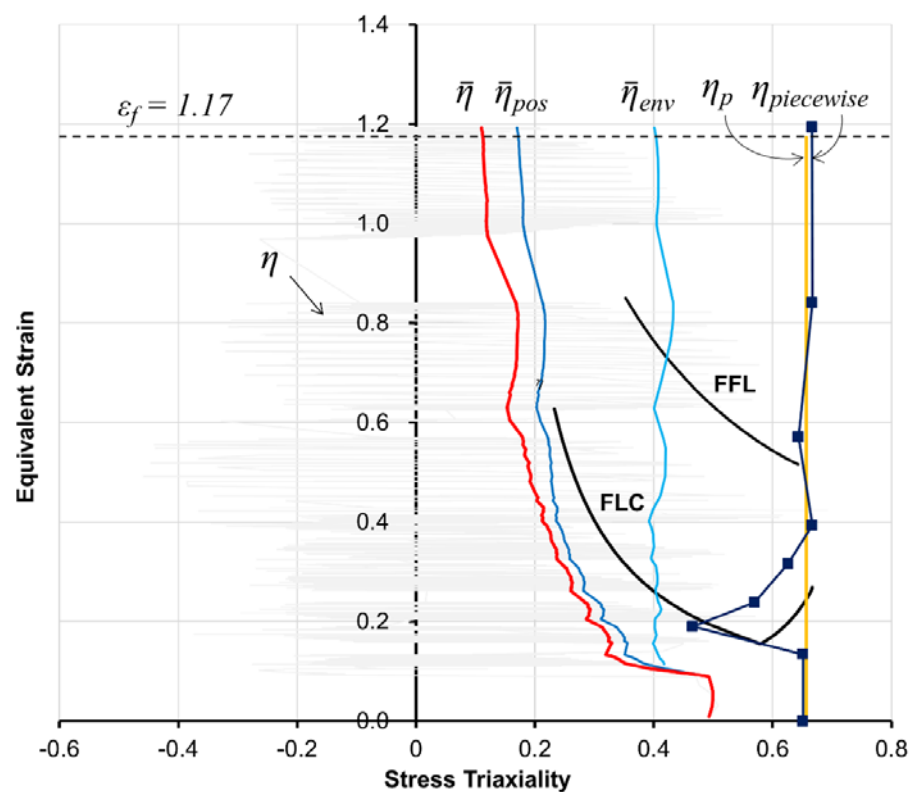


**Figure 13.** Finite element computed non-proportional, cyclic path of point A (Figure 9) with several  $\bar{\epsilon} = f(\eta)$  evolutions obtained from different assumptions and integral forms of stress-triaxiality.

As seen, the  $\bar{\epsilon} = f(\eta)$  reference evolution based on a linear, proportional, equal biaxial stress triaxiality ratio  $\eta_p$  consists of a vertical line  $\eta_p = 0.66$  that extends up to an effective strain value at fracture  $\bar{\epsilon}_f = 1.17$  located far above the FFL. The other  $\bar{\epsilon} = f(\eta)$  reference evolution based on a linear piecewise  $\eta_{piecewise}$  approximation of the experimental in-plane strains measured by ARGUS<sup>®</sup> is not very much different from that based on  $\eta_p$ . Major differences between the two evolutions are found in the forming stages 2 to 5 due to a shift in the linear piecewise  $\eta_{piecewise}$  based evolution towards plane strain.

Still, the onset of fracture at  $\bar{\epsilon}_f = 1.17$  is nearly identical to that of the  $\eta_p$  based evolution and, therefore, far above the FFL. In fact, because the linear piecewise  $\eta_{piecewise}$  based evolution is built upon a direct transformation of the experimental strain paths from

principal strain space to the effective strain vs. stress triaxiality space, it is understandable that the surpass of the FFL must occur in both spaces.

More important to our discussion are the  $\bar{\epsilon} = f(\eta)$  evolutions obtained for the integral forms of stress triaxiality given by  $\eta_{env}$ ,  $\bar{\eta}_{pos}$  and  $\bar{\eta}$  (refer to Equations (10)–(12)). As can be seen, the three evolutions reach the effective strain at fracture ( $\bar{\epsilon}_f = 1.17$ ) very far from the FFL. In particular, the evolution of  $\eta_{env}$  cuts the FFL at stress triaxiality values around 0.4, suggesting that the fracture should occur much earlier than it does. The other two ( $\bar{\eta}_{pos}$  and  $\bar{\eta}$ ) reach the fracture for values of stress triaxiality below 0.2 (i.e., in-between pure tension and pure shear) without crossing the FFL and in good agreement with a possible extrapolation of the FFL to the left side. The difference between the  $\bar{\eta}_{pos}$  and  $\bar{\eta}$  based evolutions is not relevant for incremental tube expansion and derives from discharging, or accounting for, the accumulation of negative damage. Although discharging negative damage is commonly executed in cold forming, there are studies recently published pointing to cut-off values of stress triaxiality up to  $-0.6$  for the cold forming of aluminum alloys under quasi-static loading [26]. According to this and taking into account that the instantaneous stress triaxiality in the incremental tube forming oscillates between  $-0.6$  to  $0.6$  (see Figure 13), the use of the average stress triaxiality  $\bar{\eta}$  takes on a greater physical sense.

Taking the integral form of stress triaxiality  $\bar{\eta}$  (i.e., the average stress triaxiality given by Equation (12)) into consideration, it is now important to check if the compatibility between the FFL and the above-mentioned reason for the critical in-plane strains of incremental tube expansion at fracture being far greater than those of conventional tube expansion also applies to the latter. For this purpose, we computed the  $\bar{\epsilon} = f(\eta)$  evolution for conventional tube expansion directly from the average stress triaxiality  $\bar{\eta}$  and plotted the results in Figure 14. The instantaneous stress triaxiality ( $\eta$ ) in the conventional tube expansion is also shown.

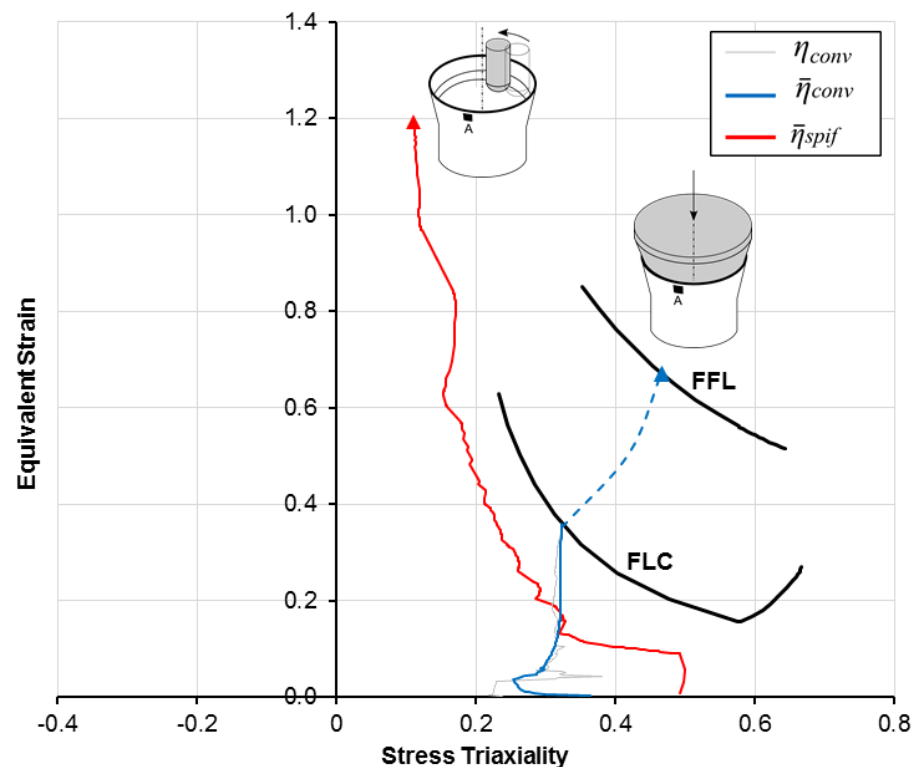


**Figure 14.** Finite element computed evolutions of the loading paths experienced by a point A located 1.5 mm away from the upper tube end in incremental and conventional tube expansion processes. Note: the red and blue triangular markers correspond to the experimentally determined “gauge length” strains at fracture.

Two interesting results can be drawn. On the one hand, the level of average stress triaxiality in the conventional process at fracture ( $\bar{\eta}_f \approx 0.47$ ) is very well above the one obtained in the incremental process ( $\bar{\eta}_f \approx 0.11$ ). As suggested by Martinez-Donaire et al. [18], this difference, also observed in other incremental forming processes [27], results in a greater resistance to accumulate damage in the incremental process than in the conventional one, requiring higher levels of strain to trigger the ductile fracture. On the other hand, results also show a near coincidence of the instantaneous and the average stress triaxiality-based evolutions ( $\eta \cong \bar{\eta}$ ) in the conventional process. This also makes sense and is compatible with the widely popular application of McClintock's ductile damage criterion [23] to determine the onset of cracking by tension in conventional tube forming processes [12]. These results confirm the validity of the overall approach for both non-proportional, cyclic paths of incremental tube expansion and near proportional paths of conventional tube expansion.

#### 4. Conclusions

The critical in-plane strains and effective strain at fracture of incremental tube expansion are greater than those of conventional tube expansion by rigid tapered conical punches. However, the conclusion that the gains in formability are due to the fact that strain paths go beyond the fracture forming limit (FFL) line of the tube material is erroneous because it does not account for the non-proportional, cyclic nature of the strain paths and because it ignores the FFL being a material property that is independent of any type of applied loading.

Finite element modelling of incremental tube expansion considering material strain hardening and non-proportional, cyclic paths resulting from the real tool trajectory combined with the utilization of appropriate integral forms of stress triaxiality allows understanding that the gains in formability result from a shift of the loading paths towards the left side in the effective strain vs. stress triaxiality space. Moreover, the results also show that this shift of material flow is of paramount importance to ensure compatibility between the critical strains at fracture and the threshold admissible values of the material FFL.

The necessity of using effective strain vs. stress triaxiality evolutions based on average stress triaxiality to ensure compatibility with the FFL in incremental tube expansion is understandable because the individual locations of the plastically deformed tube surface oscillate cyclically from shearing to biaxial stretching, as the single point hemispherical tool approaches, contacts and moves away from these locations during its trajectory.

The fact that average stress triaxiality is not required to handle the formability of conventional tube expansion is compatible with the match between stress triaxiality and the integral forms of stress triaxiality (e.g., average stress triaxiality) when material is subject to near-proportional loading paths. This last conclusion is no less important than the previous ones because it justifies the successful utilization of McClintock's fracture criterion to analyze the onset of fracture by tension in conventional tube forming processes over the past few decades.

**Author Contributions:** Conceptualization, G.C., C.V. and P.A.F.M.; methodology, M.B.S. and G.C.; software, C.S.; validation, C.S. and G.C.; formal analysis, G.C. and M.B.S.; investigation, C.S., M.B.S. and G.C.; resources, C.V., M.B.S. and P.A.F.M.; writing—original draft preparation, C.S. and G.C.; supervision, G.C. and C.V.; project administration, G.C. and C.V.; funding election and management, G.C. All authors have read and agreed to the published version of the manuscript.

**Funding:** The authors would like to express their gratitude for the funding received through the Grant number US-1263138 US/JUNTA/FEDER\_UE within "Proyectos I+D+i FEDER Andalucía 2014-2020" and the Fundação para a Ciência e da Tecnologia of Portugal, through IDMEC under LAETA, project UIDB/50022/2020.

**Institutional Review Board Statement:** Not applicable.

**Informed Consent Statement:** Not applicable.

**Data Availability Statement:** Not applicable.

**Acknowledgments:** The authors would like to acknowledge the collaborations of Jaime Blanco Vital in the preliminary development of the numerical modeling and Valentino Cristino in the experimentation.

**Conflicts of Interest:** The authors declare no conflict of interest.

## References

1. Keeler, S.P. Circular grid system—A valuable aid for evaluating sheet metal formability. In *SAE Transactions*; SAE International: Warrendale, PA, USA, 1968.
2. Goodwin, G.M. Application of strain analysis to sheet metal forming problems in the press shop. In *SAE Transactions*; SAE International: Warrendale, PA, USA, 1968.
3. Embury, J.D.; Duncan, J.L. Formability Maps. *Annu. Rev. Mater. Sci.* **1981**, *11*, 505–521. [[CrossRef](#)]
4. Centeno, G.; Martínez-Donaire, A.J.; Morales-Palma, D.; Vallellano, C.; Silva, M.B.; Martins, P.A.F. Novel experimental techniques for the determination of the forming limits at necking and fracture. *Mater. Form. Mach. Res. Dev.* **2015**, *2*, 1–24.
5. Nielsen, C.V.; Martins, P.A.F. *Metal Forming: Formability, Simulation, and Tool Design*; Elsevier Academic Press: Cambridge, MA, USA, 2021.
6. Isik, K.; Silva, M.B.; Tekkaya, A.E.; Martins, P.A.F. Formability limits by fracture in sheet metal forming. *J. Mater. Process. Technol.* **2014**, *214*, 1557–1565. [[CrossRef](#)]
7. Liu, S.D.; Meuleman, D.; Thompson, K. Analytical and experimental examination of tubular hydroforming limits. *J. Mater. Manuf.* **1998**, *107*, 287–297.
8. Chen, X.; Yu, Z.; Hou, B.; Li, S.; Lin, Z. A theoretical and experimental study on forming limit diagram for a seamed tube hydroforming. *J. Mater. Process. Technol.* **2011**, *211*, 2012–2021. [[CrossRef](#)]
9. Centeno, G.; Silva, M.B.; Alves, L.M.; Vallellano, C.; Martins, P.A.F. Towards the characterization of fracture in thin-walled tube forming. *Int. J. Mech. Sci.* **2016**, *119*, 12–22. [[CrossRef](#)]
10. Cristino, V.A.; Magrinho, J.P.; Centeno, G.; Silva, M.B.; Martins, P.A. A digital image correlation based methodology to characterize formability in tube forming. *J. Strain Anal. Eng. Des.* **2019**, *54*, 139–148. [[CrossRef](#)]
11. Magrinho, J.P.; Centeno, G.; Silva, M.B.; Vallellano, C.; Martins, P.A.F. On the formability limits of thin-walled tube inversion using different die fillet radii. *Thin-Walled Struct.* **2019**, *144*, 106328. [[CrossRef](#)]
12. Magrinho, J.P.; Silva, M.B.; Centeno, G.; Moedas, F.; Vallellano, C.; Martins, P.A.F. On the determination of forming limits in thin-walled tubes. *Int. J. Mech. Sci.* **2019**, *155*, 380–391. [[CrossRef](#)]
13. Magrinho, J.P.; Silva, M.B.; Martins, P.A.F. On the Characterization of Fracture Loci in Thin-Walled Tube Forming. In *Forming the Future, Proceedings of the 13th International Conference on the Technology of Plasticity, Pittsburgh, PA, USA, 25–30 July 2021*; Springer International Publisher: Berlin/Heidelberg, Germany, 2021.
14. Wen, T.; Yang, C.; Zhang, S.; Liu, L. Characterization of deformation behavior of thin-walled tubes during incremental forming: A study with selected examples. *Int. J. Adv. Manuf. Technol.* **2015**, *78*, 1769–1780. [[CrossRef](#)]
15. Movahedinia, H.; Mirnia, M.J.; Elyasi, M.; Baseri, H. An investigation on flaring process of thin-walled tubes using multistage single point incremental forming. *Int. J. Adv. Manuf. Technol.* **2018**, *94*, 867–880. [[CrossRef](#)]
16. Cristino, V.A.; Magrinho, J.P.; Centeno, G.; Silva, M.B.; Martins, P.A.F. Theory of single point incremental forming of tubes. *J. Mater. Process. Technol.* **2021**, *287*, 116659. [[CrossRef](#)]
17. Vujovic, V.; Shabaik, A.H. A new workability criterion for ductile metals. *J. Eng. Mater. Technol. Trans. ASME* **1986**, *108*, 245–249. [[CrossRef](#)]
18. Martínez-Donaire, A.J.; García-Lomas, F.J.; Vallellano, C. New approaches to detect the onset of localised necking in sheets under through-thickness strain gradients. *Mater. Des.* **2014**, *57*, 135–145. [[CrossRef](#)]
19. Martínez-Donaire, A.J.; Borrego, M.; Morales-Palma, D.; Centeno, G.; Vallellano, C. Analysis of the influence of stress triaxiality on formability of hole-flanging by single-stage SPIF. *Int. J. Mech. Sci.* **2019**, *151*, 76–84. [[CrossRef](#)]
20. Guglielmi, P.; Cusanno, A.; Bagudanch, I.; Centeno, G.; Ferrer, I.; Garcia-Romeu, M.L.; Palumbo, G. Experimental and numerical analysis of innovative processes for producing a resorbable cheekbone prosthesis. *J. Manuf. Process.* **2021**, *70*, 1–14. [[CrossRef](#)]
21. Centeno, G.; Martínez-Donaire, A.J.; Bagudanch, I.; Morales-Palma, D.; Garcia-Romeu, M.L.; Vallellano, C. Revisiting formability and failure of AISI304 sheets in SPIF: Experimental approach and numerical validation. *Metals* **2017**, *7*, 513. [[CrossRef](#)]
22. Mirnia, M.J.; Shamsari, M. Numerical prediction of failure in single point incremental forming using a phenomenological ductile fracture criterion. *J. Mater. Process. Technol.* **2017**, *244*, 17–43. [[CrossRef](#)]
23. McClintock, F.A. A Criterion for Ductile Fracture by the Growth of Holes. *J. Appl. Mech.* **1968**, *35*, 363–371. [[CrossRef](#)]
24. Atkins, A.G. Fracture in forming. *J. Mater. Process. Technol.* **1996**, *56*, 609–618. [[CrossRef](#)]
25. Martins, P.A.F.; Bay, N.; Tekkaya, A.E.; Atkins, A.G. Characterization of fracture loci in metal forming. *Int. J. Mech. Sci.* **2014**, *83*, 112–123. [[CrossRef](#)]

- 
26. Brüning, M.; Gerke, S.; Schmidt, M. Damage and failure at negative stress triaxialities: Experiments, modeling and numerical simulations. *Int. J. Plast.* **2018**, *102*, 70–82. [[CrossRef](#)]
  27. López-Fernández, J.A.; Centeno, G.; Martínez-Donaire, A.J.; Morales-Palma, D.; Vallellano, C. Stretch-flanging of AA2024-T3 sheet by single-stage SPIF. *Thin-Walled Struct.* **2021**, *160*, 107338. [[CrossRef](#)]